

Assessment of climate change trends over the Loess Plateau in China from 1901 to 2100

Shouzhang Peng,^{a,b} Chengcheng Gang,^{a,b} Yang Cao^{a,b} and Yunming Chen^{a,b*}

^a State Key Laboratory of Soil Erosion and Dryland Farming on the Loess Plateau, Northwest A&F University, Yangling, China

^b Institute of Soil and Water Conservation, Chinese Academy of Sciences and Ministry of Water Resources, Yangling, China

ABSTRACT: The Loess Plateau (LP) in China is sensitive to climate change because of its fragile ecological environment and geographic features. This study presents a detailed assessment of the climate change trends over the LP from 1901 to 2100 based on the 1-km spatial resolution climate data generated through delta downscaling. The following results are drawn: (1) Delta downscaling performs well in detecting the monthly precipitation and temperature over the LP based on the mean absolute error between downscaled data and independent surface observations. Among the 28 general circulation models, the GFDL-ESM2M and NorESM1-M models show the best performance in reproducing the monthly precipitation and temperature in the future period, respectively. (2) The annual precipitation over the entire LP shows no significant trends in the historical and future periods. By contrast, the annual temperature shows a significantly increasing trend with 0.097 °C/10 year in the historical period (1901–2014) and with 0.113, 0.24, 0.355, and 0.558 °C/10 year in the future period (2015–2100) under the RCP2.6, RCP4.5, RCP6.0, and RCP8.5 scenarios, respectively. (3) The significantly increasing trends in precipitation and temperature at each grid of the LP present various spatial distributions in terms of their magnitude. The significant trend magnitude calculated by the downscaled data has a larger range and a higher percentage of area – and is even observed at a small area – compared with that calculated by the raw data. (4) The spatial results calculated by the downscaled data provide more detailed information about the locations and percentages of area, both of which are valuable in assessing the change trends in precipitation and temperature. These spatio-temporal results present the climate change trends over the LP in detail and provide valuable insights for developing flexible adaptation and mitigation strategies to address the climate change challenges in this region.

KEY WORDS climate change; delta downscaling; Mann–Kendall trend test; Sen’s slope estimator; Loess Plateau

Received 26 March 2017; Revised 10 September 2017; Accepted 30 September 2017

1. Introduction

Climate change is at the forefront of scientific issues and poses a significant challenge to human survival and development, especially in China (Wang and Chen, 2014). The Loess Plateau (LP) in China is the most developed loess region in the world in terms of extent, thickness, and depositional sequence; it has an area of approximately 0.64×10^6 km² and assumes important service functions in China in terms of ecology and economy (Chen *et al.*, 2015). Over the last 50 years, the annual precipitation has decreased and the air temperature has increased over the LP (Bi *et al.*, 2009; Wang *et al.*, 2012; Sun *et al.*, 2015). These changes can damage the LP by altering its water availability and increasing the instances of soil erosion, droughts, and floods (Miao *et al.*, 2016). Thus, the climate change patterns in the LP in the historical and future periods must be understood to develop suitable adaptation and mitigation strategies that can address the challenges resulting from these changes.

General circulation models (GCMs) provide valuable information on long-term climate projections at a global to sub-continental scale (IPCC, 2013). The World Climate Research Program’s Coupled Model Intercomparison Project Phase 5 (CMIP5) provides a state-of-the-art multi-model data set that has been used by the Intergovernmental Panel on Climate Change for its fifth assessment report. Improved models of CMIP5 are expected to perform better than those of the former phase CMIP3 (Taylor *et al.*, 2012). For example, CMIP5 models have smaller bias than CMIP3 models in reproducing the atmospheric downwards long-wave radiation (Ma *et al.*, 2014) and precipitation over China (Chen and Frauenfeld, 2014). Despite showing improvements over CMIP3 models, CMIP5 models still show remarkable biases in depicting regional climate information. Previous studies (Chen *et al.*, 2012; Zhou *et al.*, 2014) have identified significant errors in the magnitude and trend of precipitation and surface air temperature at a regional scale. Thus, to reduce the biases in climate change, the existing global climate data sets, such as the Climate Research Unit (CRU) (Harris *et al.*, 2014) 0.5° time series data set, can be interpolated with weather station records when climate change information in the historical period is available.

* Correspondence to: Y. Chen, Institute of Soil and Water Conservation, Chinese Academy of Sciences and Ministry of Water Resources, No. 26, Xinong Road, Yangling, Shaanxi 712100, China. E-mail: ymchen@ms.iswc.ac.cn; or E-mail: szp@nwafu.edu.cn

Most of the present-day GCMs have a horizontal resolution of a few hundred kilometres (Meehl *et al.*, 2007). Efforts have been made to downscale the CMIP3 and CMIP5 model data sets to 0.5° (i.e. approximately 55 km) across the globe (Brekke *et al.*, 2013). However, similar to the CRU data set, spatial resolution continues to limit the capability of GCM data sets to represent complex topography, land surface characteristics, and other processes in the climate system (Xu *et al.*, 2017). This condition also prevents the GCM and CRU data sets from drawing realistic and reliable climate change information at fine scales, which is imperative when developing suitable adaptation and mitigation strategies at the regional to local scales (Giorgi *et al.*, 2009). Therefore, downscaling a climate data set using a dynamic downscaling model (i.e. regional climate model) for GCM data or using a statistical downscaling model for GCM and CRU data is necessary because these models add the orographic effects and calibrations of observed records to the data (Mosier *et al.*, 2014; Xu *et al.*, 2017), which may reduce the uncertainties in the raw data. Although dynamic downscaling can provide a mechanism for interpreting regional climate change and output many climate variables, this technique requires numerous inputs and computational requirements (Brekke *et al.*, 2013; Xu *et al.*, 2017) and sometimes cannot present reliable climate change information at fine scales (Dosio *et al.*, 2015; Xu *et al.*, 2017). Besides, to date, statistical downscaling can provide a climate data set with a 1-km spatial resolution (Mosier *et al.*, 2014), which is hardly generated by dynamic downscaling. Thus, statistical downscaling can be adopted to generate a high-spatial-resolution climate dataset in the LP region.

Previous studies (Bi *et al.*, 2009; Li *et al.*, 2010; Li *et al.*, 2012b; Wang *et al.*, 2012; Miao *et al.*, 2016) have assessed the climate change trends over the LP in terms of near-surface air temperature and precipitation in the historical and future periods. However, these studies have been conducted at a station scale (Bi *et al.*, 2009; Li *et al.*, 2010; Wang *et al.*, 2012) or at a 0.5° spatial resolution (Miao *et al.*, 2016). Moreover, the climate change information in the historical period has only been monitored beginning in the 1960s, and most weather stations in China have been established around that time. Long time series of detailed spatial variations of climate change trends in the region are largely unavailable, and such information is important in developing flexible adaptation and mitigation strategies that can address the climate change issues in the LP.

The objectives of this study are (1) to generate historical and future temperature and precipitation data over the LP with a high-spatio-temporal resolution by applying the statistical downscaling method on CRU and GCM data; (2) to detect whether the downscaled data have a higher reliability than the raw CRU and GCM data; and (3) to assess the historical and future climate change trends and their spatial variations over the LP based on the raw/downscaled climate data from 1901 to 2100.

2. Data and methods

2.1. Study area

The LP region is situated in north China (33.7° – 41.3° N, 100.8° – 114.6° E) and traversed by the upper-middle reaches of the Yellow River (Figure 1). The region starts from the TaiHang Mountains in the east, reaches the RiYue Mountain in the west, and borders on the QinLing Mountains in the south and Yin Mountain in the north (Liu *et al.*, 2016). The LP has a warm or temperate continental monsoon climate with extensive monsoonal influence. The annual precipitation ranges from 200 mm in the northwest to 750 mm in the southeast (Li *et al.*, 2012b), 60–70% of which falls from June to September in the form of high-intensity storms (Wang *et al.*, 2012). The annual mean temperature ranges from 3.6° C in the northwest to 14.3° C in the southeast. A large diurnal temperature range is observed throughout the year with dry and cold winters, hot and humid summers, rapid temperature decrease in autumn, and rapid temperature increase in spring. The annual potential evaporation, which ranges from 865 to 1274 mm, in this area is estimated to be much higher than the precipitation (Li *et al.*, 2012a). The region spans arid, semi-arid, and semi-humid zones and is considered a semi-arid-to-semi-humid transitional zone that is sensitive to climate change (Liu and Sang, 2013).

2.2. Data collection

The historical monthly precipitation and mean temperature data used in this study were obtained from the CRU TS 3.23 data set with a 0.5° spatial resolution (Harris *et al.*, 2014). This data set presents the data for January 1901 to December 2014 in a time series. The GCM monthly precipitation and mean temperature data used in this study were obtained from the downscaled CMIP5 data set with a 0.5° resolution (http://gdo-dcp.ucllnl.org/downscaled_cmip_projections/). This data set was processed from 28 raw GCMs data using the bias correction and delta downscaling methods described by Brekke *et al.* (2013). Table 1 lists the basic information on the 28 models and their associated institutions. This data set presents the data for January 1950 to December 2100 in a time series; the data from 1950 to 2005 are the historical data under the historical emissions scenario, while the data from 2006 to 2100 are the future data under the future Representative Concentration Pathway (RCP) scenarios (i.e. RCP2.6, RCP4.5, RCP6.0, and RCP8.5 scenarios).

The high-resolution reference climatology data used in this study were gridded data on a 1-km (approximately 30 arcseconds) resolution as elaborated by the Chinese National Ecosystem Research Network (CNERN, www.cnern.org.cn). These climatology data were processed by using spatial interpolation and geographic information systems with 740 national weather stations in China and a 1-km digital elevation model (DEM). These high-resolution reference climatology data, which covered each month of the years 1961–2000, include the orographic effects and calibrations of observed climate information records for each month.

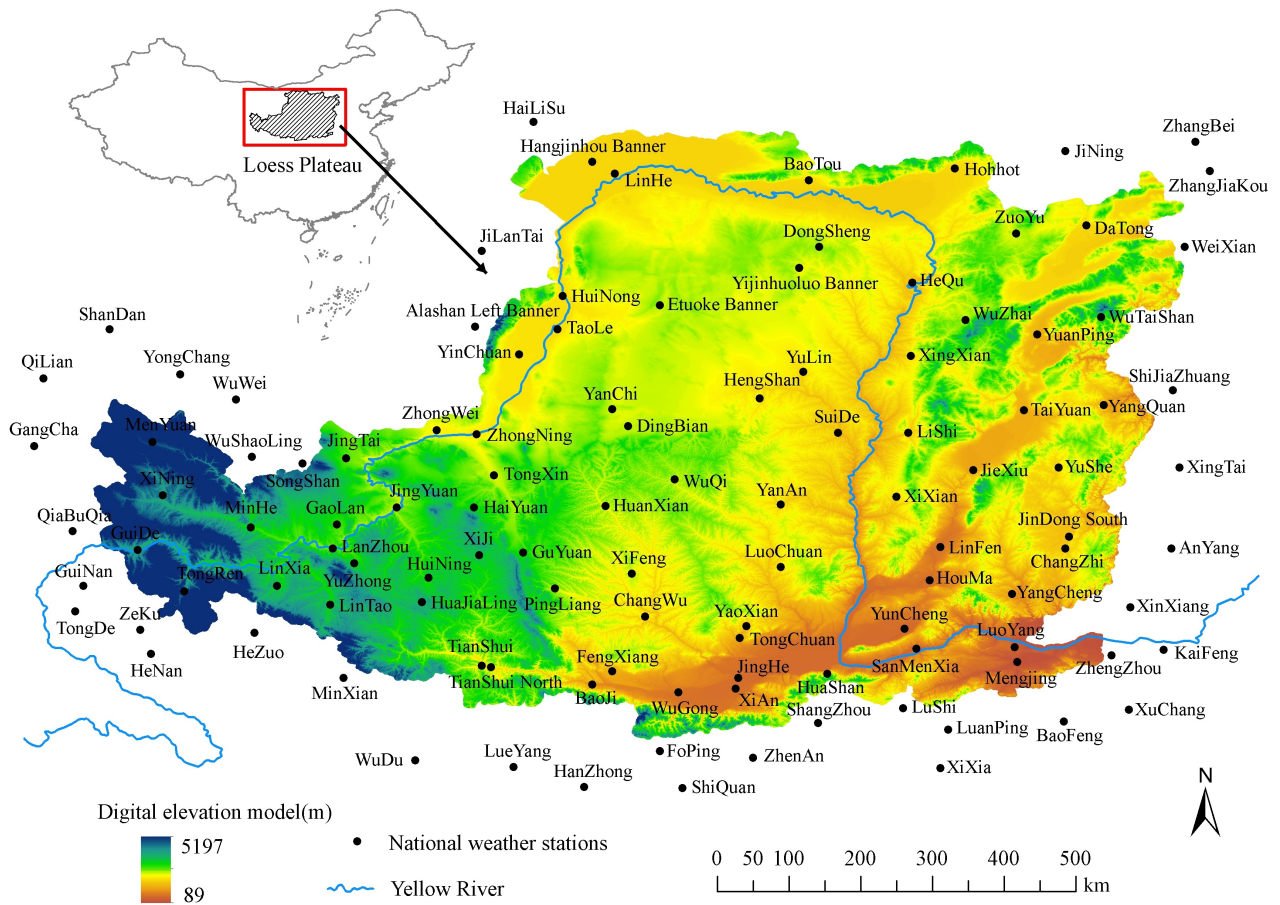


Figure 1. Location and DEM of the LP region in China and 113 national weather stations distributed across the rectangular region. [Colour figure can be viewed at wileyonlinelibrary.com].

The surface observation data for monthly precipitation and mean temperature were obtained from 113 national weather stations in and around the LP (Figure 1; <http://data.cma.cn/>); these data were used to evaluate the downscaled monthly precipitation and mean temperature grids from January 1991 to December 2014 in a time series (period of the available data).

2.3. Statistical downscaling

The statistical downscaling framework includes regression and delta downscaling methods. The regression method constructs multiple linear regression relationships between the raw GCM data and station observations in the historical period; these relationships are applied to future GCM grid outputs (Li *et al.*, 2012b; Timm *et al.*, 2015). This framework can generate substantial climate element data in the future at target stations but cannot obtain a future climate dataset with a high spatial resolution, thereby preventing the drawing of detailed spatial variations at fine scales. Meanwhile, the delta downscaling method uses a low-resolution monthly time series and high-resolution reference climatology as inputs; the high-resolution climatology input must contain a physically representative, fine-scale distribution of the meteorological variable over the landscape (Brekke *et al.*, 2013; Mosier *et al.*, 2014). Instead of directly interpolating low-spatial-resolution

sources (such as CRU and GCM data) to a higher spatial resolution, delta downscaling incorporates high-resolution orographic effects in the reference climatology that are not represented in low-resolution input grids (Mosier *et al.*, 2014). Furthermore, instead of interpolation that considers high-spatial-resolution DEM for CRU and GCM data, delta downscaling incorporates calibrations of observed records from multiple stations in the reference climatology.

Delta downscaling is used with the data described in the preceding section to produce monthly precipitation and mean temperature grids for the years 1901–2100 with a 1-km resolution. Figure 2 shows a rectangular region (Figure 1) that includes the LP region to illustrate the components and steps of delta downscaling for precipitation by using the CRU 0.5° time series and CNERN 30-arcsecond climatology data sets. The first step (Figure 2(a)) is to construct a 0.5° climatology for each month from the 0.5° time series data set. The low-resolution climatology is produced using the period 1961–2000 because this range is used by CNERN to construct its climatology data. A 0.5° anomaly (Figure 2(b)) is then calculated. The anomaly for precipitation is calculated as the ratio of the time series element to the corresponding low-resolution climatology, while the anomaly for temperature is calculated as the difference between the time series element and climatology. The

Table 1. Summary of the 28 general circulation models from CMIP5.

	Model acronym	Institution	References
1	ACCESS1.0	Commonwealth Scientific and Industrial Research Organization and Bureau of Meteorology, Australia	Marsland <i>et al.</i> (2013)
2	BCC-CSM1.1	Beijing Climate Center, China Meteorological Administration, China	Xin <i>et al.</i> (2013)
3	BCC-CSM1.1(m)	Beijing Climate Center, China Meteorological Administration, China	Ren <i>et al.</i> (2016)
4	BNU-ESM	Beijing Normal University, China	Ji <i>et al.</i> (2014)
5	CanESM2	Canadian Centre for Climate Modelling and Analysis, Canada	Chylek <i>et al.</i> (2011)
6	CESM1-BGC	NSF/DOE NCAR, United States	Long <i>et al.</i> (2013)
7	CESM1-CAM5	NSF/DOE NCAR, United States	Neale <i>et al.</i> (2013)
8	CMCC-CM	Centro Euro-Mediterraneo per I Cambiamenti Climatici, Italy	Scoccimarro <i>et al.</i> (2011)
9	CNRM-CM5	Centre National de Recherches Meteorologiques, Météo-France, France	Voldoire <i>et al.</i> (2013)
10	CSIRO-MK-3.6.0	Australian Commonwealth Scientific and Industrial Research Organization, Australia	Rotstayn <i>et al.</i> (2010)
11	EC-EARTH	EC-EARTH consortium, Europe	Hazeleger <i>et al.</i> (2012)
12	FGOALS-g2	Institute of Atmospheric Physics, Chinese Academy of Sciences, China	Zhou <i>et al.</i> (2013)
13	FIO-ESM	The First Institution of Oceanography, SOA, China	Qiao <i>et al.</i> (2013)
14	GFDL-CM3	NOAA Geophysical Fluid Dynamics Laboratory, United States	Donner <i>et al.</i> (2011)
15	GFDL-ESM2G	NOAA Geophysical Fluid Dynamics Laboratory, United States	Dunne <i>et al.</i> (2012)
16	GFDL-ESM2M	NOAA Geophysical Fluid Dynamics Laboratory, United States	Dunne <i>et al.</i> (2012)
17	GISS-E2-H-CC	NASA Goddard Institute for Space Studies, United States	Wang <i>et al.</i> (2015)
18	GISS-E2-R	NASA Goddard Institute for Space Studies, United States	Schmidt <i>et al.</i> (2006)
19	GISS-E2-R-CC	NASA Goddard Institute for Space Studies, United States	Wang <i>et al.</i> (2015)
20	HadCM3	Met Office Hadley Centre, UK	Collins <i>et al.</i> (2001)
21	INMCM4.0	Institute for Numerical Mathematics, Russia	Volodin <i>et al.</i> (2010)
22	IPSL-CM5A-LR	Institut Pierre–Simon Laplace, France	Dufresne <i>et al.</i> (2013)
23	MIROC4h	Japan Agency for Marine–Earth Science and Technology, University of Tokyo, and National Institute for Environmental Studies (Japan)	Zhang <i>et al.</i> (2017)
24	MIROC5	Japan Agency for Marine–Earth Science and Technology, University of Tokyo, and National Institute for Environmental Studies (Japan)	Watanabe <i>et al.</i> (2010)
25	MIROC-ESM	Japan Agency for Marine–Earth Science and Technology, University of Tokyo, and National Institute for Environmental Studies (Japan)	Watanabe <i>et al.</i> (2011)
26	MIROC-ESM-CHEM	Japan Agency for Marine–Earth Science and Technology, University of Tokyo, and National Institute for Environmental Studies (Japan)	Watanabe <i>et al.</i> (2011)
27	MRI-CGCM3	Meteorological Research Institute, Japan	Yukimoto <i>et al.</i> (2012)
28	NorESM1-M	Norwegian Climate Centre, Norway	Bentsen <i>et al.</i> (2013)

anomaly is then interpolated to the 30-arcsecond CNERN grid through spatial interpolation (Figure 2(c)). The final step in the delta method (Figure 2(d)) is transforming the high-resolution anomaly back to an absolute surface by scaling it using the CNERN climatology for the corresponding month. This transformation undoes the creation of the anomaly; therefore, multiplication is used for precipitation, while addition is used for temperature.

As illustrated in Figure 2(c), the anomaly grid can be interpolated from the original to the high-resolution coordinates by using many interpolation methods. Thus, the delta downscaling framework not only employs

the interpolation method but also introduces the high-resolution reference climatology data. The use of such data represents the biggest difference between the delta downscaling and statistical interpolation methods. This study compared the nearest-neighbour interpolation, bilinear interpolation, cubic spline interpolation, and bicubic interpolation (Mosier *et al.*, 2014), and applied these interpolation methods using the `interp2` function in Matlab.

2.4. Evaluation of delta downscaling

Spatial downscaling was conducted over the rectangular region in Figure 1. The surface observation records

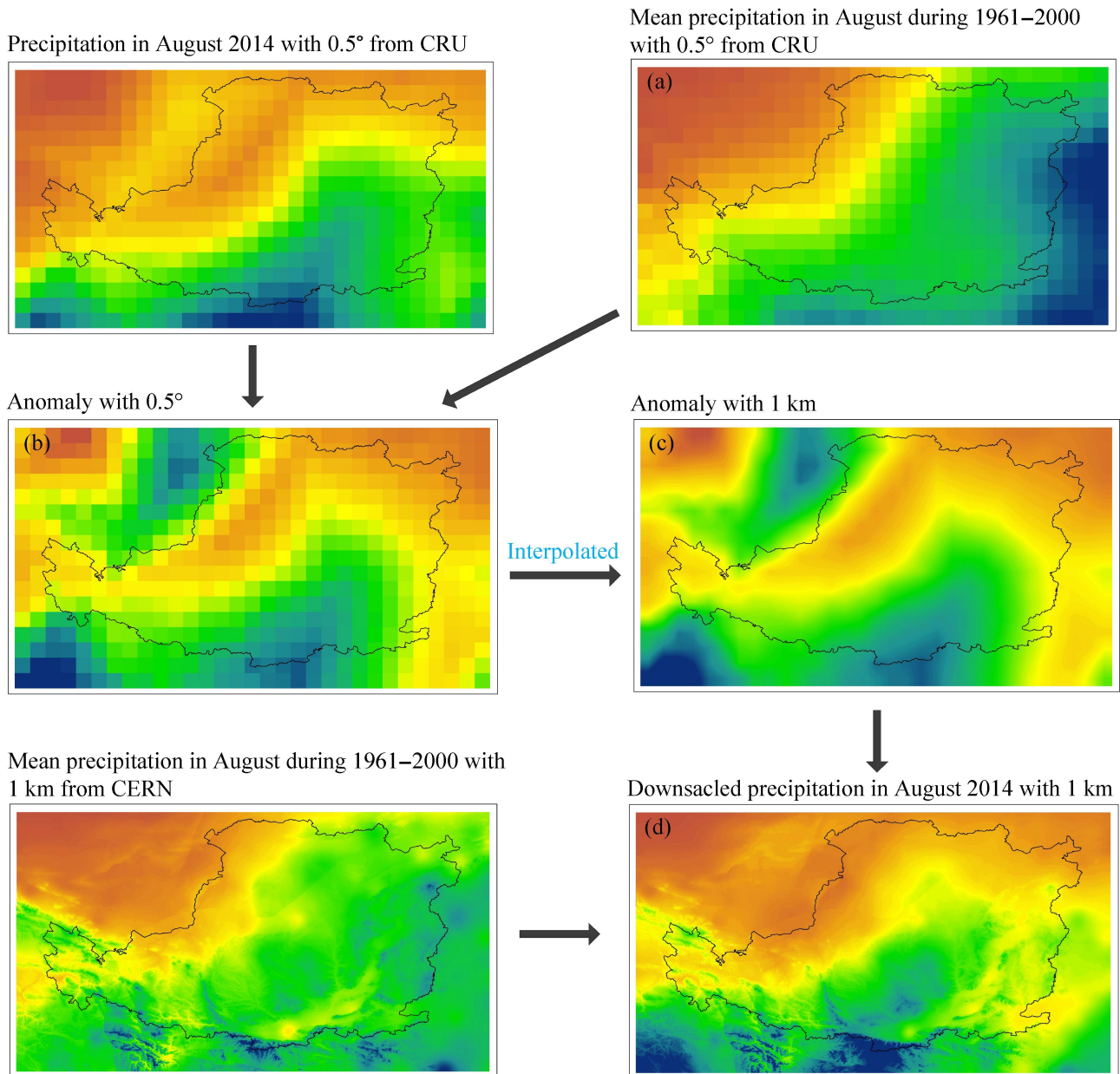


Figure 2. Schematic illustration of the spatial downscaling process. The downscaled precipitation field is constructed from CRU data in August 2014. [Colour figure can be viewed at wileyonlinelibrary.com].

from the 113 national weather stations across the rectangular region were used to independently verify the accuracy of the downscaled grids. The observation records covering January 2001 to December 2014 were used to verify the downscaled results from the CRU data, while the observation records covering January 1991 to December 2005 were used to verify the downscaled results from the GCM data. These observed records were also used to verify the raw CRU and GCM data during the same periods.

The average model performance error was quantified by the mean absolute error (MAE), which is a more natural measure of average error than the root-mean-square error (Willmott and Matsuura, 2005; Wang and Chen, 2014). This accuracy estimator can be mathematically written as:

$$\text{MAE} = \frac{1}{n} \sum_{i=1}^n |P_i - O_i| \quad (1)$$

where P_i is the downscaled or raw value, O_i is the observed value, and n is the number of records of all validated stations.

2.5. Trend analysis methods

The tests for detecting significant trends in climatologic time series can be classified as either parametric or nonparametric. Parametric trend tests require independent and normally distributed data, while nonparametric trend tests only require independent data (Gocic and Trajkovic, 2013). We used two nonparametric methods (Mann–Kendall and Sen's slope estimator) to detect the

Table 2. MAE of raw/downscaled monthly mean temperature and precipitation from 28 GCMs in January 1991 to December 2005 and CRU in January 2001 to December 2014.

	Monthly precipitation (mm)					Monthly temperature (°C)				
	Np	Bic	Bil	Near	Spl	Np	Bic	Bil	Near	Spl
ACCESS1-0	24.22	23.44	23.38	23.46	23.44	2.968	1.460	1.458	1.462	1.460
BCC-CSM1-1	24.71	23.92	23.89	23.94	23.92	2.877	1.419	1.418	1.419	1.419
BCC-CSM1-1-m	24.38	23.65	23.60	23.69	23.65	2.963	1.449	1.447	1.450	1.449
BNU-ESM	24.14	23.31	23.28	23.33	23.31	2.888	1.429	1.429	1.430	1.429
CanESM2	26.72	25.58	25.53	25.59	25.58	2.741	1.363	1.361	1.364	1.363
CESM1-BGC	24.94	23.23	23.16	23.27	23.23	2.942	1.434	1.432	1.435	1.434
CESM1-CAM5	24.00	23.27	23.20	23.30	23.27	2.875	1.392	1.390	1.392	1.392
CMCC-CM	24.75	24.05	23.99	24.08	24.05	3.142	1.484	1.482	1.484	1.484
CNRM-CM5	24.60	23.85	23.80	23.89	23.85	3.177	1.451	1.449	1.451	1.451
CSIRO-MK-3-6-0	23.44	22.60	22.54	22.59	22.60	3.045	1.424	1.422	1.425	1.424
EC-EARTH	25.34	24.66	24.60	24.71	24.66	3.089	1.444	1.442	1.444	1.444
FGOALS-g2	24.39	23.63	23.59	23.67	23.63	3.100	1.470	1.469	1.470	1.470
FIO-ESM	24.86	23.66	23.63	23.68	23.66	3.179	1.534	1.533	1.535	1.534
GFDL-CM3	24.44	23.66	23.63	23.71	23.66	2.993	1.383	1.382	1.384	1.384
GFDL-ESM2G	24.58	23.82	23.78	23.88	23.82	2.947	1.415	1.413	1.416	1.415
GFDL-ESM2M	23.09	22.39	22.35	22.43	22.39	2.969	1.425	1.423	1.426	1.425
GISS-E2-H-CC	24.70	23.94	23.90	23.99	23.94	3.056	1.499	1.498	1.500	1.499
GISS-E2-R	23.87	23.13	23.09	23.17	23.13	2.777	1.347	1.346	1.347	1.347
GISS-E2-R-CC	24.53	23.81	23.78	23.86	23.81	2.952	1.407	1.406	1.407	1.407
HadCM3	23.71	22.89	22.85	22.90	22.89	3.214	1.505	1.503	1.507	1.505
inmcm4	24.64	23.87	23.82	23.89	23.87	3.310	1.564	1.562	1.565	1.564
IPSL-CM5A-LR	24.11	23.24	23.20	23.25	23.24	3.307	1.549	1.548	1.550	1.549
MIROC4h	23.88	23.07	22.97	23.15	23.08	3.004	1.471	1.469	1.472	1.471
MIROC5	23.00	22.97	22.92	23.00	22.97	2.907	1.446	1.445	1.447	1.446
MIROC-ESM	25.50	24.68	24.63	24.69	24.68	2.888	1.379	1.377	1.380	1.379
MIROC-ESM-CHEM	24.67	23.93	23.89	23.94	23.93	3.384	1.600	1.599	1.600	1.600
MRI-CGCM3	25.07	24.14	24.09	24.17	24.15	3.335	1.571	1.570	1.571	1.571
NorESM1-M	24.05	23.16	23.12	23.18	23.17	2.713	1.343	1.342	1.344	1.343
CRU	15.16	14.27	14.25	14.28	14.27	1.665	0.801	0.798	0.806	0.801

Np represents the MAE between the raw GCM/CRU and observed data; Bic, Bil, Near, and Spl represent the bicubic, bilinear, nearest-neighbour, and cubic spline interpolations used in the downscaled framework, respectively.

trends of the raw and downscaled climate data in each grid over the LP. The Mann–Kendall trend test provides a measure (Z_{MK}) that indicates whether the long-term change of a variable is significant (Atta-ur-Rahman and Dawood, 2017). This study conducted a comparison analysis at the 95% confidence level. The trend of the time series is significant at the 95% confidence level when $|Z_{MK}| > 1.96$. $Z_{MK} > 1.96$ denotes a significant increase, while $Z_{MK} < -1.96$ denotes a significant decrease. The magnitude of temperature or precipitation trend was calculated by the Sen's slope estimator test (Atta-ur-Rahman and Dawood, 2017).

3. Results

3.1. Evaluation of raw/downscaled temperature and precipitation

Table 2 shows the MAE between the raw/downscaled and observed monthly climate data. For CRU and each GCM data, the MAE of the raw data is slightly greater than that of the downscaled data. In the delta-downscaled framework, the MAE under the bilinear interpolation is always the smallest for the CRU and GCMs data. Specifically, among the 28 GCMs, the GFDL-ESM2M and NorESM1-M models have the smallest MAE in reproducing the

monthly precipitation and mean temperature over the LP, respectively. Thus, these data for these two models can be used to generate the high-spatial-resolution future climate data in the delta downscaling framework. In addition, the MAE of the raw/downscaled CRU data is smaller than that of each raw/downscaled GCM data. Thus, the CRU data must be selected to generate the high-spatial-resolution historical climate data in the delta downscaling framework.

Figures 3 and 4 compare the observed and raw/downscaled values of monthly precipitation and mean temperature; the raw/downscaled values of GCM data are processed from the GFDL-ESM2M and NorESM1-M models. The regression and correlation coefficients show that (1) the downscaled data are closer to the observed values than the raw CRU and GCM data; (2) compared with the downscaled precipitation data, the downscaled temperature data are closer to the observed temperature values for both CRU and GCM data; and (3) the CRU data are closer to the observed values than the GCM data for both downscaled and raw precipitation and temperature data.

3.2. Trends in precipitation

We used bilinear interpolation to downscale the CRU and suitable GCM (i.e. GFDL-ESM2M and NorESM1-M models) data over the LP for 1901–2100 to 1-km spatial

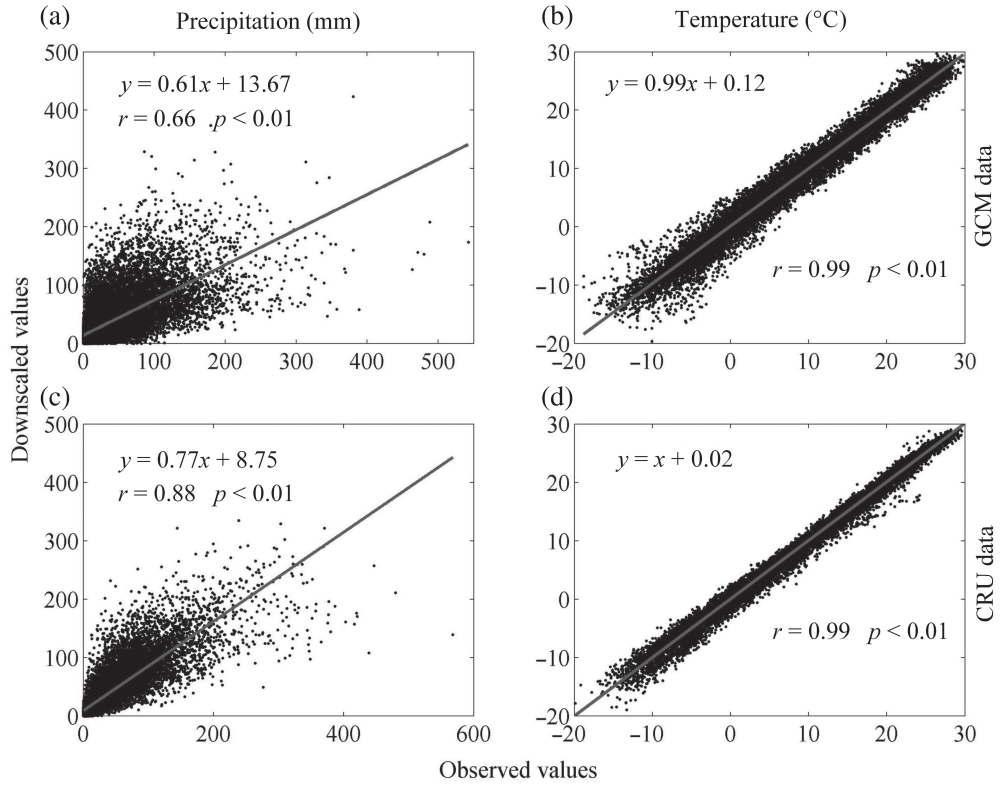


Figure 3. Comparisons of the observed (x) and downsampled (y) values of monthly precipitation and mean temperature. The downsampled monthly precipitation (a) and mean temperature (b) values are obtained from GFDL-ESM2M and NorESM1-M models, respectively.

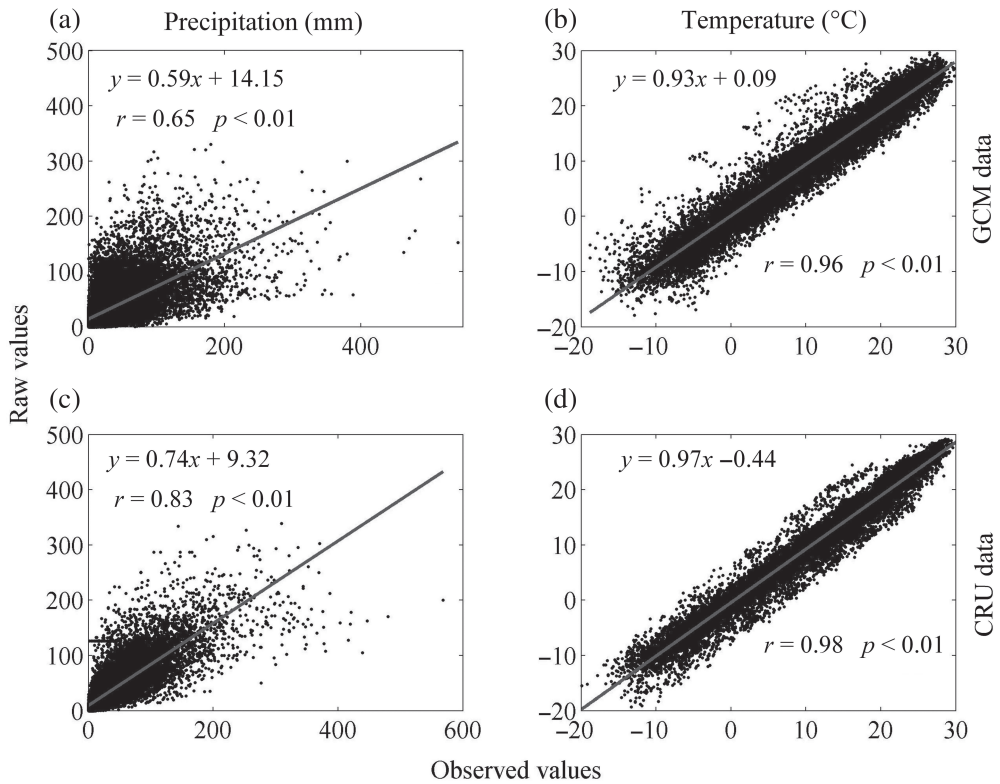


Figure 4. Comparisons of the observed (x) and raw (y) values of monthly precipitation and mean temperature. The raw monthly precipitation (a) and mean temperature (b) values are obtained from GFDL-ESM2M and NorESM1-M models, respectively.

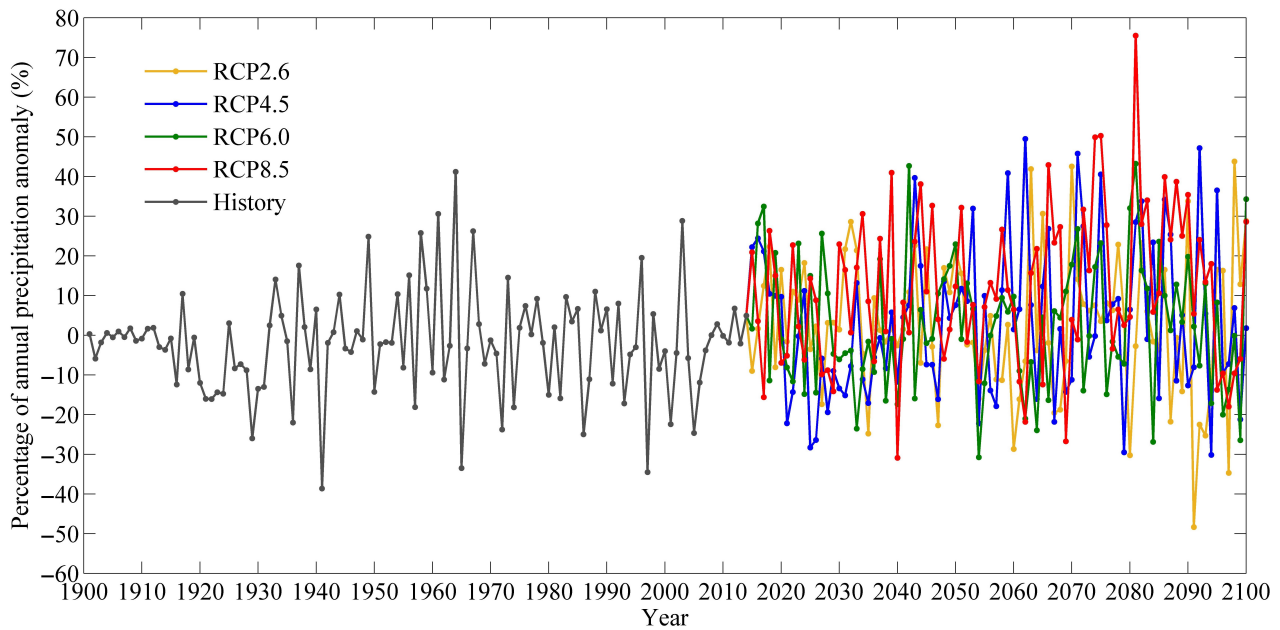


Figure 5. Change in annual precipitation of the entire LP from the reference period (1961–1990) to the historical and future periods (1901–2100), where 1901–2014 is the historical period and 2015–2100 is the future period. [Colour figure can be viewed at [wileyonlinelibrary.com](#)].

resolution. The data during 1901–2014 were taken from CRU and the data during 2015–2100 were taken from the GFDL-ESM2M and NorESM1-M models. Based on the downscaled monthly precipitation data, we calculated the anomalies of annual precipitation over the LP region. Relative to that during 1961–1990, the anomaly during the historical period (1901–2014) ranges from -36.8 to 41.2% , while that during the future period (2015–2100) ranges from -48.5 to 75.5% under the four RCP scenarios (Figure 5). No significant differences were found between the historical and future fluctuations in annual precipitation (Figure 5). The Mann–Kendall test shows no significant trends in the historical and future annual precipitation over the entire LP using the raw/downscaled data.

To detect the detailed spatial variation of trends in annual precipitation over the LP using the raw/downscaled data, we performed Mann–Kendall and Sen's slope estimator tests at each grid. Figure 6 shows the spatial distribution of the magnitude of trend during the historical period (i.e. 114-year span) using the downscaled data. Although this magnitude presents a strong spatial variation over the LP region, a significantly increasing trend is only observed in the west of the LP region (Figure 6). Furthermore, the corresponding magnitude ranges from 0.24 to 3.52 mm/10 year with a mean of 1.76 mm/10 year in the zones with a significant trend, and these zones cover 3.10% of the LP region (Table 3). Compared with the significant trend magnitude calculated by the downscaled data, that calculated by the raw data has a narrower range (0.67 – 1.4 mm/10 year), lower mean (1.08 mm/10 year), and lower percentage of area (2.72%), although their coefficients of variability are nearly the same (Table 3).

Figure 7 shows the spatial distribution of the magnitude of trend during the future period (i.e. 86-year span) under the four RCP scenarios using the downscaled data. A

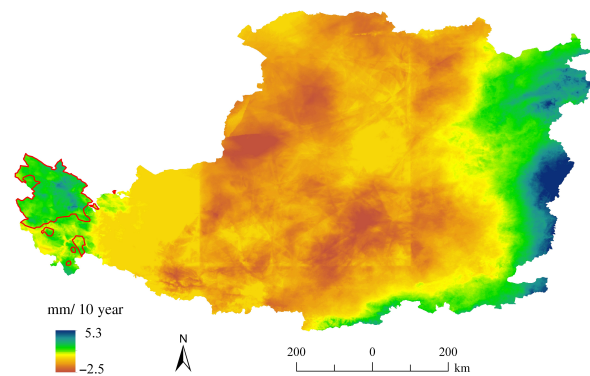


Figure 6. Geographic distribution of the magnitude of trend for annual precipitation (mm/10 year) in the historical period (1901–2014). The closed solid line indicates where the trend significantly increases at the 95% confidence level. [Colour figure can be viewed at [wileyonlinelibrary.com](#)].

significantly increasing trend is only observed in the south of the LP with a 9.32% area under the RCP4.5 scenario and in the west of the LP with a 0.14% area under the RCP8.5 scenario (Figure 7). The corresponding magnitude ranges from 7.06 to 41.11 mm/10 year with a mean of 13.81 mm/10 year under the RCP4.5 scenario and from 5.2 to 9.9 mm/10 year with a mean of 6.6 mm/10 year under the RCP8.5 scenario (Table 3). In addition, the magnitude under the RCP 4.5 scenario (22.65%) has a greater spatial variation than that under the RCP8.5 scenario (10.71%), while the magnitude during the historical period has a greater spatial variation (26.81%) than that during the future period (Table 3). Compared with the significant trend magnitude calculated by the downscaled data, that calculated by the raw data under the RCP4.5 scenario has a narrower range (8.63 – 14.08 mm/10 year), lower mean

Table 3. Summary of minimum (Min, mm/10 year), maximum (Max, mm/10 year), mean (Mean, mm/10 year), standard deviation (SD, mm/10 year), coefficient of variability (CV), and percentage of area (PA) for the spatial distribution of the significant trend in annual precipitation during the historical and future periods.

		1901–2014	2015–2100			
			RCP2.6	RCP4.5	RCP6.0	RCP8.5
Min	Raw	0.67	–	8.63	–	–
	Downscaled	0.24	–	7.06	–	5.15
Max	Raw	1.40	–	14.08	–	–
	Downscaled	3.52	–	41.11	–	9.86
Mean	Raw	1.08	–	10.40	–	–
	Downscaled	1.76	–	13.81	–	6.58
SD	Raw	0.29	–	2.31	–	–
	Downscaled	0.47	–	3.13	–	0.71
CV	Raw	26.55%	–	22.23%	–	–
	Downscaled	26.81%	–	22.65%	–	10.71%
PA	Raw	2.72%	–	8.17%	–	–
	Downscaled	3.10%	–	9.32%	–	0.14%

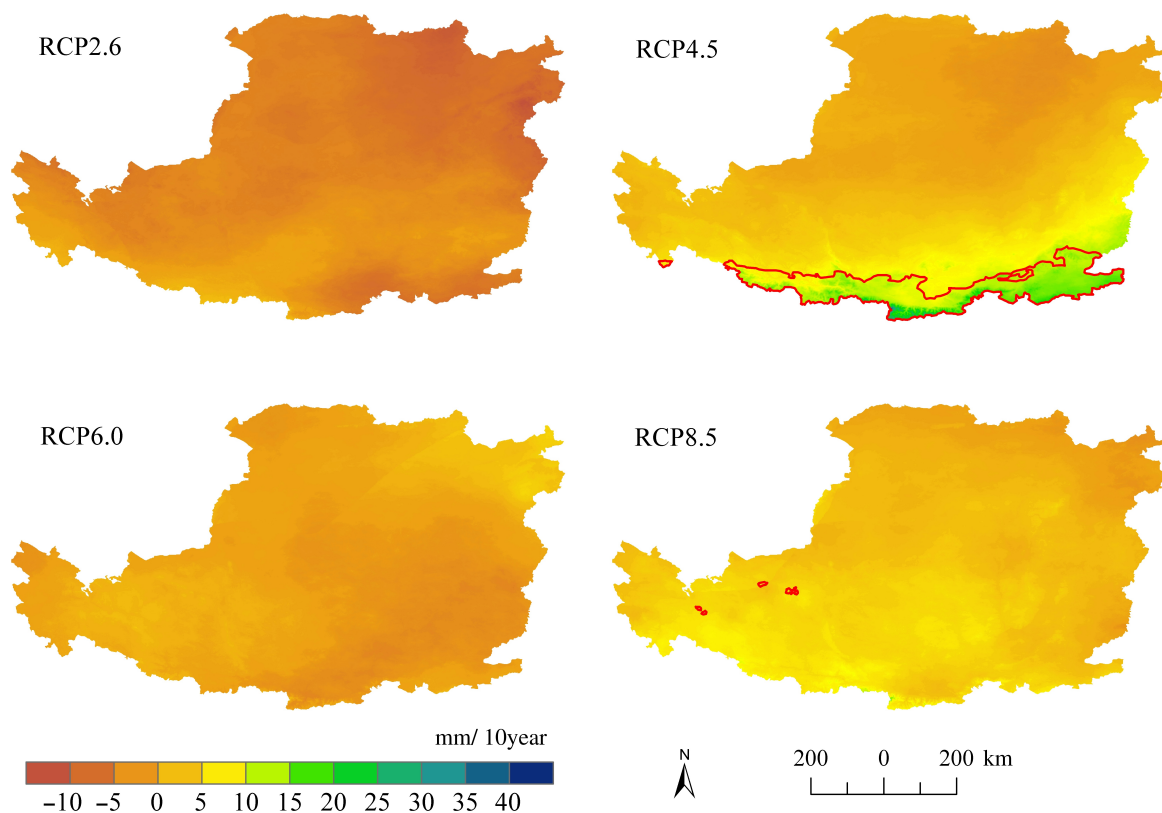


Figure 7. Geographic distribution of the magnitude of trend for annual precipitation (mm/10 year) in the future period (2015–2100) under the four RCP scenarios. The closed solid line indicates where the trend significantly increases at the 95% confidence level. [Colour figure can be viewed at wileyonlinelibrary.com].

(10.4 mm/10 year), and lower percentage of area (8.17%), although their coefficients of variability are nearly the same (Table 3). Besides, the Mann–Kendall test shows no significant trend for the raw precipitation data over the entire LP under the RCP8.5 scenario (Table 3).

3.3. Trends in mean temperature

Similar to precipitation, we calculated the anomalies of annual mean temperature over the LP region based on the downscaled data and then performed Mann–Kendall and

Sen's slope estimator tests for the annual mean temperature at each grid on the basis of the raw/downscaled data.

Relative to that during 1961–1990, the anomalies during the historical period (1901–2014) range from -0.992 to 1.843 °C (Figure 8). Meanwhile, the anomalies during the future period (2015–2100) range from 0.016 to 3.046 °C with a mean of 1.878 °C under the RCP2.6 scenario, from 0.545 to 4.125 °C with a mean of 2.390 °C under the RCP4.5 scenario, from 0.382 to 4.468 °C with a mean of 2.393 °C under the RCP6.0 scenario, and

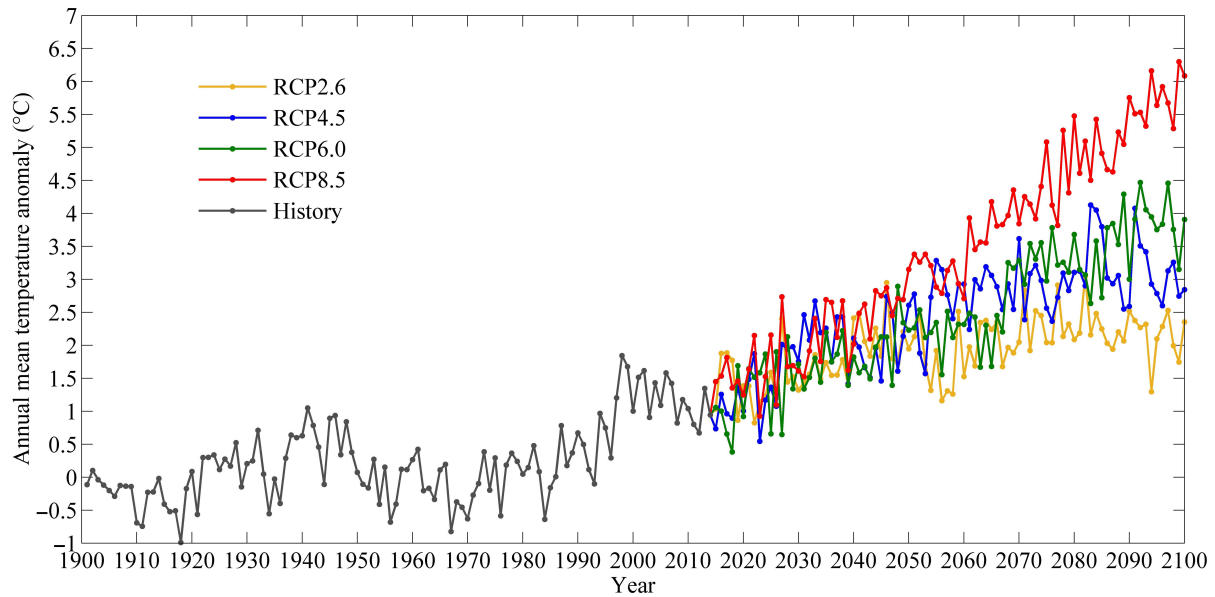


Figure 8. Change in annual mean temperature of the entire LP from the reference period (1961–1990) to the historical and future periods (1901–2100), where 1901–2014 is the historical period and 2015–2100 is the future period. [Colour figure can be viewed at wileyonlinelibrary.com].

from 0.52 to 6.296 °C with a mean of 3.318 °C under the RCP8.5 scenario (Figure 8). Furthermore, the annual mean temperature of the LP region based on the down-scaled data presents a significantly increasing trend with 0.097 °C/10 year in the historical period and with 0.113, 0.24, 0.355, and 0.558 °C/10 year in the future period under the RCP2.6, RCP4.5, RCP6.0, and RCP8.5 scenarios, respectively. The significant trend calculated by the raw data presents almost the same magnitudes as that calculated by the down-scaled data.

Figure 9 shows the spatial distribution of the magnitude of trend for the annual mean temperature during the historical period based on the down-scaled data. A significantly increasing trend is observed in the zone apart from the west over the LP region (Figure 9). The corresponding magnitude ranges from 0.021 to 0.172 °C/10 year with a mean of 0.106 °C/10 year in the zone with a significant trend, and this zone covers 91.30% of the LP region (Table 4). Compared with the significant trend magnitude calculated by the down-scaled data, that calculated by the raw data has a narrower range (0.026–0.167 °C/10 year) and lower percentage of area (90.27%) although their coefficients of variability and mean are nearly the same (Table 4).

Compared with those in the historical period, the significantly increasing trends in the future period have a greater percentage of area and magnitude of trend based on the down-scaled data (Figure 10 and Table 4). The corresponding percentages of area are 97.80% under the RCP2.6 scenario and 100% under the RCP4.5, RCP6.0, and RCP8.5 scenarios (Table 4). The corresponding magnitude ranges from 0.026 to 0.150 °C/10 year with a mean of 0.114 °C/10 year under the RCP2.6 scenario, from 0.179 to 0.306 °C/10 year with a mean of 0.243 °C/10 year under the RCP4.5 scenario, from 0.283 to 0.405 °C/10 year with a mean of 0.355 °C/10 year under the RCP6.0 scenario,

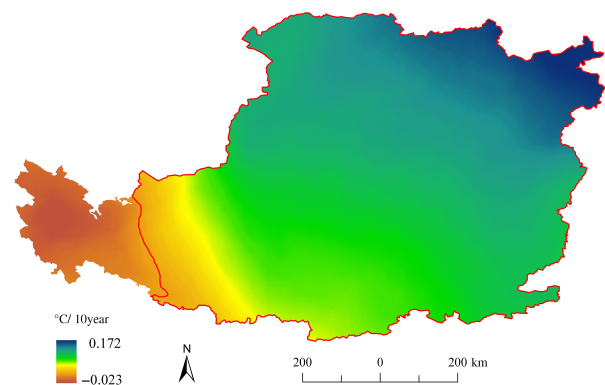


Figure 9. Geographic distribution of the magnitude of trend for annual mean temperature (°C/10 year) in the historical period (1901–2014). The closed solid line indicates where the trend significantly increases at the 95% confidence level. [Colour figure can be viewed at wileyonlinelibrary.com].

and from 0.505 to 0.623 °C/10 year with a mean of 0.558 °C/10 year under the RCP8.5 scenario (Table 4). In addition, the magnitude during the historical period has a greater spatial variation (26.83%) than that during the future period under the four RCP scenarios (19.38, 12.29, 7.69, and 5.52%; Table 4). Compared with the significant trend magnitude calculated by the down-scaled data under each RCP scenario, that calculated by the raw data has a narrower range and lower/equal percentage of area although their averaged values are nearly the same (Table 4).

4. Discussion

This study evaluated the performances of raw and down-scaled climate data sets using observed records and then

Table 4. Summary of minimum (Min, °C/10 year), maximum (Max, °C/10 year), mean (Mean, °C/10 year), standard deviation (SD, °C/10 year), coefficient of variability (CV), and percentage of area (PA) for the spatial distribution of the significant trend in annual temperature during the historical and future periods.

		1901–2014	2015–2100			
			RCP2.6	RCP4.5	RCP6.0	RCP8.5
Min	Raw	0.026	0.032	0.181	0.285	0.507
	Downscaled	0.021	0.026	0.179	0.283	0.505
Max	Raw	0.167	0.146	0.297	0.400	0.620
	Downscaled	0.172	0.150	0.306	0.405	0.623
Mean	Raw	0.107	0.112	0.243	0.354	0.558
	Downscaled	0.106	0.114	0.243	0.355	0.558
SD	Raw	0.029	0.028	0.030	0.028	0.031
	Downscaled	0.029	0.022	0.030	0.027	0.031
CV	Raw	26.87%	24.85%	12.40%	7.86%	5.59%
	Downscaled	26.83%	19.38%	12.29%	7.69%	5.52%
PA	Raw	90.27%	96.89%	100%	100%	100%
	Downscaled	91.30%	97.80%	100%	100%	100%

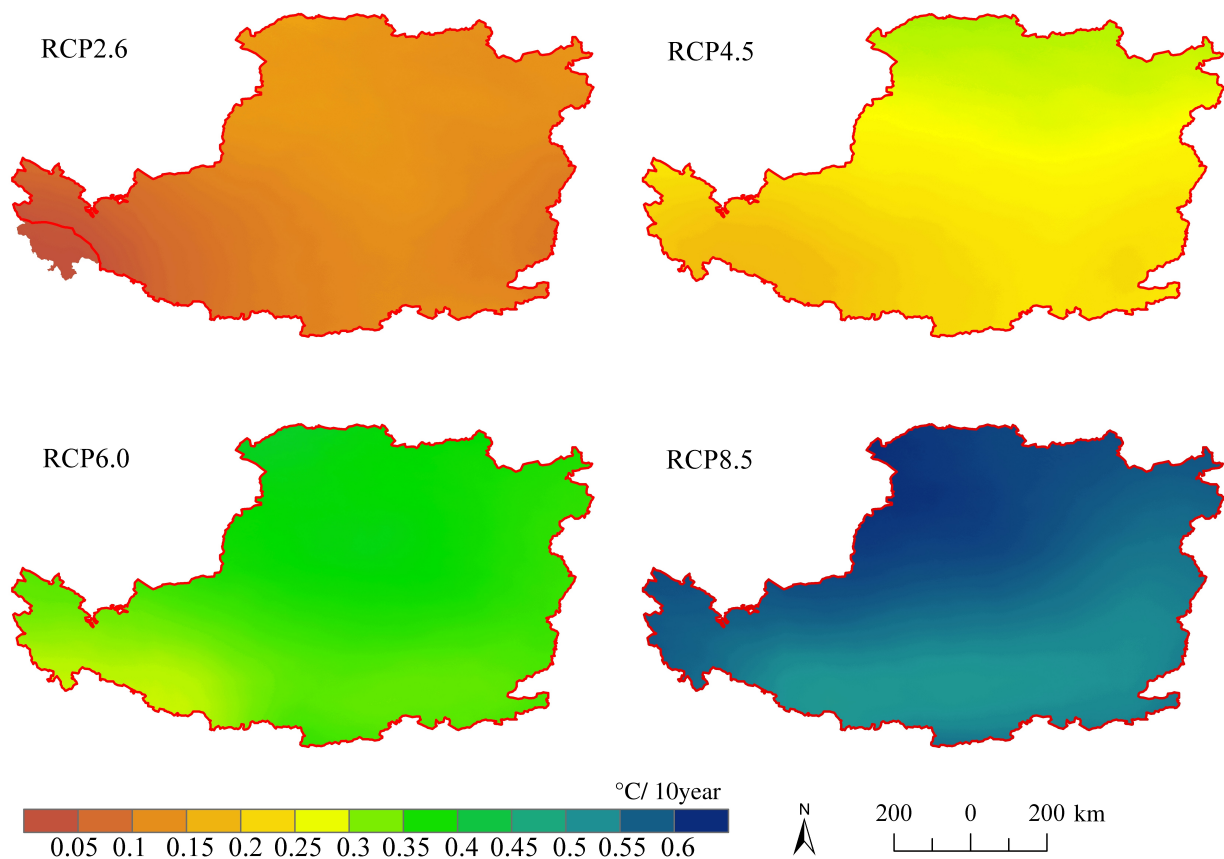


Figure 10. Geographic distribution of the magnitude of trend for annual mean temperature (°C/10 year) in the future period (2015–2100) under the four RCP scenarios. The closed solid line indicates where the trend significantly increases at the 95% confidence level. [Colour figure can be viewed at wileyonlinelibrary.com].

detected the climate trends based on these two data sets. The MAE of raw data is always higher than that of the downscaled data for the CRU and 28 GCMs data sets (Table 2). This result implies that the delta downscaling framework not only produces highly detailed climate information at the fine scale but also reduces the uncertainties in the CRU and 28 GCMs data sets. This finding can be attributed to the orographic effects and the

calibrations of observed records from multiple stations in the high-spatial-resolution reference climatology data. The significant trend magnitude calculated by the downscaled data has a larger range and higher percentage of area – and is even present at a small area – compared with that calculated by the raw data (Tables 3 and 4). These results imply that the downscaled data not only represent high-spatial-resolution climate trends but are also more

reliable than the raw data for studying climate trends. Therefore, the downscaled data are more reasonable than the raw data for studying climate trends.

This study employed delta downscaling to generate monthly precipitation and mean temperature data with a 1-km spatial resolution from January 1901 to December 2100 by using the CRU and 28 GCM data sets with a 0.5° spatial resolution and the high-resolution climatology representing the orographic effect. The MAE between the downscaled data and the independent surface station observations indicates that delta downscaling performs well in the study area. Wang and Chen (2014) used the delta method to downscale 35 raw GCMs data to a 0.5° spatial resolution in China; the MAE ranged from 10 to 80 mm with a mean of approximately 50 mm for monthly precipitation and from 1.6 to 5.7 °C with a mean of approximately 3.2 °C for monthly mean temperature. Compared with that in Wang and Chen (2014), the MAE in the present study is smaller and ranges from 22.35 to 25.53 mm with a mean of 23.58 mm for monthly precipitation and from 1.342 to 1.600 °C with a mean of roughly 1.45 °C for monthly mean temperature (Table 2). Wang and Chen (2014) also showed that the model with the smallest MAE was EC-EARTH, which is used to generate the 0.5°-spatial-resolution temperature and precipitation in China. The GFDL-ESM2M and NorESM1-M models in the present study show the best results in reproducing the monthly precipitation and mean temperature over the LP, respectively, on the basis of the MAE analysis. These differences may be attributed to the fact that in this study, the high-resolution climatology with a 1-km spatial resolution was adopted for downscaling and the surface station observations were used to evaluate the downscaled results. This comparison implies that the selections of high-resolution climatology and evaluation data are crucial when the delta downscaling framework is adopted. Currently, WorldClim (Mosier *et al.*, 2014) and the climatology employed in this study remain the best available high-resolution climatologies (1-km spatial resolution) in the world and in China, respectively.

Compared with precipitation, the temperature over the entire LP region has a larger fluctuation and shows a more significantly increasing trend in the historical and future periods (Figures 5 and 8). Specifically, in the historical period, the west of the LP region showed significantly increasing trends in annual precipitation and insignificant trends in annual mean temperature, while the zones apart from the west in the LP presented insignificant trends in annual precipitation and significantly increasing trends in annual mean temperature (Figures 6 and 9). These results imply that the zones apart from the west in the LP region suffered considerable water loss in the historical period. In the future period, the south of the LP region presented significantly increasing trends in annual precipitation under the RCP4.5 scenario (Figure 7), and most of the LP region presented significantly increasing trends in annual mean temperature under the four RCP scenarios (Figure 10). These results imply that the zones apart from the south in the LP region will suffer considerable water loss in the future period. Such water shortage in the historical and

future periods may threaten the native vegetation ecosystem in the region, and the necessary adaptation and mitigation strategies must be adopted to address this threat.

The magnitudes of precipitation and temperature trends in the historical and future periods demonstrate a very strong spatial variability (Tables 3 and 4). The significant trends in precipitation and temperature are mapped over the LP, and their distributions present diverse characteristics, especially in terms of location and percentage of area (Figures 6, 7, 9, and 10). The findings of delta downscaling reveal that the above detailed spatial results differ from those presented in other climate change studies that have mapped the climate variables (e.g. temperature and precipitation) on the basis of the data from multiple weather stations and by using geo-statistical interpolation methods, such as inverse distance weighted interpolation (Li *et al.*, 2012a) and ordinary kriging interpolation (Atta-ur-Rahman and Dawood, 2017). Overall, unlike those from other studies, the spatial results in the present study can be used to draw the detailed orographic effects on temperature and precipitation as well as to generate highly accurate information, such as location, percentage of area, and other statistical indexes. The significant temperature and precipitation trends in the future period under the four RCP scenarios also show diverse spatial patterns and statistical results (Figures 7 and 10 and Tables 3 and 4). The comparison among the three major uncertainties in climate predictions that result from future natural fluctuations, model responses, and emission scenarios (Hawkins and Sutton, 2011) suggests that the above diversity can be attributed to the uncertainties of various scenarios (Ning and Bradley, 2016). In this study, the uncertainty of the significantly increasing temperature trends increases along with the emission scenarios, with the largest spread being observed under the RCP8.5 scenario.

The trend magnitude may also depend on the time subsection. For instance, during the 1901–2014 period, the annual mean temperature and annual precipitation over entire LP region present a significantly increasing trend with 0.097 °C/10 year (Figure 8) and a non-significantly increasing trend with 0.46 mm/10 year (Figure 5), respectively; however, the climate trends in the LP region based on the observed records show that the annual mean temperature presents a significantly increasing trend with 0.38 °C/10 year during the 1961–2010 period, while the annual precipitation presents a non-significantly decreasing trend with 5.82 mm/10 year during the same period (Wang *et al.*, 2012). We also calculate the climate trends during the 1961–2010 period, and the annual mean temperature and annual precipitation over the entire LP region present a significantly increasing trend with 0.366 °C/10 year and a non-significantly decreasing trend with 4.48 mm/10 year. The findings of Wang *et al.* (2012) almost match our results. Therefore, time subsection is an important factor in determining climate trends. Besides, compared with the spatial distribution of trend magnitude studied by Wang *et al.* (2012) using weather station data, the spatial results in this study that are obtained using downscaled data can present highly

detailed information, including location, percentage of area, and spatial variability.

5. Conclusions

This study presented a detailed assessment of the climate change trends over the LP in the historical and future periods (1901–2100) on the basis of the high-spatio-temporal-resolution climate data generated through delta downscaling. The major findings are outlined as follows:

- (1) The delta downscaling framework not only generates highly detailed climate information at the fine scale but also reduces the uncertainties in the CRU and GCMs data sets. Among the 28 GCMs, the GFDL-ESM2M and NorESM1-M models are deemed the most suitable for reproducing the future monthly precipitation and mean temperature over the LP, respectively.
- (2) The downscaled data not only represent high-spatial-resolution climate trends but are also more reliable than the raw data for studying the climate trends over the LP region.
- (3) The significantly increasing trends in precipitation and temperature present various spatial distributions in their magnitudes. The spatial results provide information on locations and percentages of area, which are valuable in assessing precipitation and temperature change trends.
- (4) Compared with precipitation, the temperature over the entire LP region shows a larger fluctuation and a more significantly increasing trend in the historical and future periods. The zones apart from the west in the LP region suffered from considerable water loss in the historical period, while the zones apart from the south in the LP region will suffer considerable water loss in the future period. Necessary adaptation and mitigation strategies must be adopted to address these issues.

Acknowledgements

This work was supported by National Natural Science Foundation of China (41601058 and 31602004), CAS ‘Light of West China’ Program (XAB2015B07), China Special Fund for Meteorological Research in the Public Interest (major projects) (GYHY201506001-3), and key cultivation project of Chinese Academy of Sciences ‘The promotion and management of ecosystem functions of restored vegetation in Loess Plateau, China’. The authors are grateful to the World Climate Research Programme’s Working Group on Coupled Modelling, which is responsible for CMIP, and the authors thank the climate modeling groups (listed in Table 1) for producing and making available their model output. For CMIP the US Department of Energy’s Program for Climate Model Diagnosis and Intercomparison provides coordinating support and led development of software infrastructure in partnership with the Global Organization for Earth System Science Portals.

In addition, the authors wish to thank two anonymous reviewers for their constructive suggestions to improve the quality of this article.

References

- Atta-ur-Rahman, Dawood M. 2017. Spatio-statistical analysis of temperature fluctuation using Mann–Kendall and Sen’s slope approach. *Clim. Dyn.* **48**: 783–797. <https://doi.org/10.1007/s00382-016-3110-y>.
- Bentsen M, Bethke I, Debernard JB, Iversen T, Kirkevåg A, Seland Ø, Drange H, Roelandt C, Seierstad IA, Hoose C, Kristjánsson JE. 2013. The Norwegian earth system model, NorESM1-M – Part 1: description and basic evaluation of the physical climate. *Geosci. Model Dev.* **6**: 687–720. <https://doi.org/10.5194/gmdd-5-2843-2012>.
- Bi H, Liu B, Jie W, Yun L, Chen Z, Cui Z. 2009. Effects of precipitation and landuse on runoff during the past 50 years in a typical watershed in Loess Plateau, China. *Int. J. Sediment Res.* **24**: 352–364. [https://doi.org/10.1016/S1001-6279\(10\)60009-1](https://doi.org/10.1016/S1001-6279(10)60009-1).
- Brekke L, Thrasher B, Maurer E, Pruitt T. 2013. *Downscaled CMIP3 and CMIP5 climate and hydrology projections: release of downscaled CMIP5 climate projections, comparison with preceding information, and summary of user needs*. US Department of the Interior, Bureau of Reclamation, Technical Services Center, Denver, CO. https://gdodcp.ucllnl.org/downscaled_cmip_projections/techmemo/downscaled_climate.pdf (accessed 20 October 2017).
- Chen L, Frauenfeld OW. 2014. A comprehensive evaluation of precipitation simulations over China based on CMIP5 multimodel ensemble projections. *J. Geophys. Res.* **119**: 5767–5786. <https://doi.org/10.1002/2013JD021190>.
- Chen L, Pryor S, Li D. 2012. Assessing the performance of Intergovernmental Panel on Climate Change AR5 climate models in simulating and projecting wind speeds over China. *J. Geophys. Res.* **117**: D24102. <https://doi.org/10.1029/2012JD017533>.
- Chen Y, Wang K, Lin Y, Shi W, Song Y, He X. 2015. Balancing green and grain trade. *Nat. Geosci.* **8**: 739–741. <https://doi.org/10.1038/ngeo2544>.
- Chylek P, Li J, Dubey MK, Wang M, Lesins G. 2011. Observed and model simulated 20th century Arctic temperature variability: Canadian earth system model CanESM2. *Atmos. Chem. Phys. Discuss.* **2011**: 22893–22907. <https://doi.org/10.5194/acpd-11-22893-2011>.
- Collins M, Tett SFB, Cooper C. 2001. The internal climate variability of HadCM3, a version of the Hadley Centre coupled model without flux adjustments. *Clim. Dyn.* **17**: 61–81. <https://doi.org/10.1007/s003820000094>.
- Donner LJ, Wyman BL, Hemler RS, Horowitz LW, Ming Y, Zhao M, Golaz JC, Ginoux P, Lin SJ, Schwarzkopf MD, Austin J, Alaka G, Cooke WF, Delworth TL, Freidenreich SM, Gordon CT, Griffies SM, Held IM, Hurlin WJ, Klein SA, Knutson TR, Langenhorst AR, Lee HC, Lin Y, Magi BI, Malyshev SL, Milly PCD, Naik V, Nath MJ, Pincur R, Ploshay JJ, Ramaswamy V, Seman CJ, Shevliakova E, Sirutis JJ, Stern WF, Stouffer RJ, Wilson RJ, Winton M, Wittenberg AT, Zeng F. 2011. The dynamical core, physical parameterizations, and basic simulation characteristics of the atmospheric component AM3 of the GFDL global coupled model CM3. *J. Clim.* **24**: 3484–3519. <https://doi.org/10.1175/2011jcli3955.1>.
- Dosio A, Panitz H-J, Schubert-Frisius M, Lüthi D. 2015. Dynamical downscaling of CMIP5 global circulation models over CORDEX-Africa with COSMO-CLM: evaluation over the present climate and analysis of the added value. *Clim. Dyn.* **44**: 2637–2661. <https://doi.org/10.1007/s00382-014-2262-x>.
- Dufresne J-L, Foujols MA, Denvil S, Caubel A, Marti O, Aumont O, Balkanski Y, Bekki S, Bellenger H, Benshila R, Bony S, Bopp L, Braconnot P, Brockmann P, Cadule P, Cheruy F, Codron F, Cozic A, Cugnet D, de Noblet N, Duvel JP, Ethé C, Fairhead L, Fichet T, Flavoni S, Friedlingstein P, Grandpeix JY, Guez L, Guilyardi E, Hauglustaine D, Hourdin F, Idelkadi A, Ghattas J, Joussaume S, Kageyama M, Krinner G, Labetoulle S, Lahellec A, Lefebvre MP, Lefevre F, Levy C, Li ZX, Lloyd J, Lott F, Madec G, Mancip M, Marchand M, Masson S, Meurdesoif Y, Mignot J, Musat I, Parouty S, Polcher J, Rio C, Schulz M, Swingedouw D, Szopa S, Talandier C, Teray P, Viovy N, Vuichard N. 2013. Climate change projections using the IPSL-CM5 Earth System Model: from CMIP3 to CMIP5. *Clim. Dyn.* **40**: 2123–2165. <https://doi.org/10.1007/s00382-012-1636-1>.

- Dunne JP, John JG, Adcroft AJ, Griffies SM, Hallberg RW, Shevliakova E, Stouffer RJ, Cooke W, Dunne KA, Harrison MJ, Krasting JP, Malyshev SL, Milly PCD, Philipps PJ, Sentman LT, Samuels BL, Spelman MJ, Winton M, Wittenberg AT, Zadeh N. 2012. GFDL's ESM2 global coupled climate-carbon earth system models. Part I: physical formulation and baseline simulation characteristics. *J. Clim.* **25**: 6646–6665. <https://doi.org/10.1175/jcli-d-11-00560.1>.
- Giorgi F, Jones C, Asrar GR. 2009. Addressing climate information needs at the regional level: the CORDEX framework. *World Meteorol. Org. Bull.* **58**: 175–183.
- Gocic M, Trajkovic S. 2013. Analysis of changes in meteorological variables using Mann–Kendall and Sen's slope estimator statistical tests in Serbia. *Global Planet. Change* **100**: 172–182. <https://doi.org/10.1016/j.gloplacha.2012.10.014>.
- Harris I, Jones P, Osborn T, Lister D. 2014. Updated high-resolution grids of monthly climatic observations—the CRU TS3.10 dataset. *Int. J. Climatol.* **34**: 623–642. <https://doi.org/10.1002/joc.3711>.
- Hawkins E, Sutton R. 2011. The potential to narrow uncertainty in projections of regional precipitation change. *Clim. Dyn.* **37**: 407–418. <https://doi.org/10.1007/s00382-010-0810-6>.
- Hazeleger W, Wang X, Severijns C, Ștefănescu S, Bintanja R, Sterl A, Wyser K, Semmler T, Yang S, van den Hurk B, van Noije T, van der Linden E, van der Wiel K. 2012. EC-Earth V2.2: description and validation of a new seamless Earth System Prediction Model. *Clim. Dyn.* **39**: 2611–2629. <https://doi.org/10.1007/s00382-011-1228-5>.
- IPCC. 2013. In *Climate Change 2013: The Physical Science Basis. Contribution of Working Group I to the Fifth Assessment Report of the Intergovernmental Panel on Climate Change*, Stocker TF, Qin D, Plattner G-K, Tignor M, Allen SK, Boschung J, Nauels A, Xia Y, Bex V, Midgley PM (eds). Cambridge University Press: Cambridge, UK and New York, NY.
- Ji D, Wang L, Feng J, Wu Q, Cheng H, Zhang Q, Yang J, Dong W, Dai Y, Gong D, Zhang RH, Wang X, Liu J, Moore JC, Chen D, Zhou M. 2014. Description and basic evaluation of Beijing Normal University Earth System Model (BNU-ESM) version 1. *Geosci. Model Dev.* **7**: 2039–2064. <https://doi.org/10.5194/gmd-7-2039-2014>.
- Li Z, F-L Z, W-Z L, Flanagan DC. 2010. Spatial distribution and temporal trends of extreme temperature and precipitation events on the Loess Plateau of China during 1961–2007. *Quat. Int.* **226**: 92–100. <https://doi.org/10.1016/j.quaint.2010.03.003>.
- Li Z, Zheng F, Liu W. 2012a. Spatiotemporal characteristics of reference evapotranspiration during 1961–2009 and its projected changes during 2011–2099 on the Loess Plateau of China. *Agric. For. Meteorol.* **154**: 147–155. <https://doi.org/10.1016/j.agrformet.2011.10.019>.
- Li Z, Zheng F, Liu W, Jiang D. 2012b. Spatially downscaling GCMs outputs to project changes in extreme precipitation and temperature events on the Loess Plateau of China during the 21st Century. *Global Planet. Change* **82**: 65–73. <https://doi.org/10.1016/j.gloplacha.2011.11.008>.
- Liu W, Sang T. 2013. Potential productivity of the Miscanthus energy crop in the Loess Plateau of China under climate change. *Environ. Res. Lett.* **8**: 044003.
- Liu Z, Wang Y, Shao M, Jia X, Li X. 2016. Spatiotemporal analysis of multiscalar drought characteristics across the Loess Plateau of China. *J. Hydrol.* **534**: 281–299. <https://doi.org/10.1016/j.jhydrol.2016.01.003>.
- Long MC, Lindsay K, Peacock S, Moore JK, Doney SC. 2013. Twentieth-century oceanic carbon uptake and storage in CESM1(BGC). *J. Clim.* **26**: 6775–6800. <https://doi.org/10.1175/jcli-d-12-00184.1>.
- Ma Q, Wang K, Wild M. 2014. Evaluations of atmospheric downward longwave radiation from 44 coupled general circulation models of CMIP5. *J. Geophys. Res.* **119**: 4486–4497. <https://doi.org/10.1002/2013JD021427>.
- Marsland SJ, Bi D, Uotila P, Hirst AC. 2013. Evaluation of ACCESS climate model ocean diagnostics in CMIP5 simulations. *Aust. Meteorol. Oceanogr. J.* **63**: 101–119. <https://doi.org/10.22499/2.6301.007>.
- Meehl GA, Covey C, Taylor KE, Delworth T, Stouffer RJ, Latif M, McAvaney B, Mitchell JFB. 2007. The WCRP CMIP3 multi-model dataset: a new era in climate change research. *Bull. Am. Meteorol. Soc.* **88**: 1383–1394. <https://doi.org/10.1175/BAMS-88-9-1383>.
- Miao C, Sun Q, Duan Q, Wang Y. 2016. Joint analysis of changes in temperature and precipitation on the Loess Plateau during the period 1961–2011. *Clim. Dyn.* **47**: 3221–3234. <https://doi.org/10.1007/s00382-016-3022-x>.
- Mosier TM, Hill DF, Sharp KV. 2014. 30-arcsecond monthly climate surfaces with global land coverage. *Int. J. Climatol.* **34**: 2175–2188. <https://doi.org/10.1002/joc.3829>.
- Neale RB, Richter J, Park S, Lauritzen PH, Vavrus SJ, Rasch PJ, Zhang M. 2013. The mean climate of the community atmosphere model (CAM4) in forced SST and fully coupled experiments. *J. Clim.* **26**: 5150–5168. <https://doi.org/10.1175/jcli-d-12-00236.1>.
- Ning L, Bradley RS. 2016. NAO and PNA influences on winter temperature and precipitation over the eastern United States in CMIP5 GCMs. *Clim. Dyn.* **46**: 1257–1276. <https://doi.org/10.1007/s00382-015-2643-9>.
- Qiao F, Song Z, Bao Y, Song Y, Shu Q, Huang C, Zhao W. 2013. Development and evaluation of an earth system model with surface gravity waves. *J. Geophys. Res.* **118**: 4514–4524. <https://doi.org/10.1002/jgrc.20327>.
- Ren HL, Wu J, Zhao CB, Cheng YJ, Liu XW. 2016. MJO ensemble prediction in BCC-CSM1.1(m) using different initialization schemes. *Atmos. Oceanic Sci. Lett.* **9**: 60–65. <https://doi.org/10.1080/16742834.2015.1116217>.
- Rotstayn LD, Collier MA, Dix MR, Feng Y, Gordon HB, O'Farrell SP, Smith IN, Syktus J. 2010. Improved simulation of Australian climate and ENSO-related rainfall variability in a global climate model with an interactive aerosol treatment. *Int. J. Climatol.* **30**: 1067–1088. <https://doi.org/10.1002/joc.1952>.
- Schmidt GA, Ruedy R, Hansen JE, Aleinov I, Bell N, Bauer M, Bauer S, Cairns B, Canuto V, Cheng Y, del Genio A, Faluvegi G, Friend AD, Hall TM, Hu Y, Kelley M, Kiang NY, Koch D, Lacis AA, Lerner J, Lo KK, Miller RL, Nazarenko L, Oinas V, Perlwitz J, Perlwitz J, Rind D, Romanou A, Russell GL, Sato M, Shindell DT, Stone PH, Sun S, Tausnev N, Thresher D, Yao MS. 2006. Present-day atmospheric simulations using GISS ModelE: comparison to in situ, satellite, and reanalysis data. *J. Clim.* **19**: 153–192. <https://doi.org/10.1175/jcli3612.1>.
- Scoccimarro E, Gualdi S, Bellucci A, Sanna A, Giuseppe Fogli P, Manzini E, Vichi M, Oddo P, Navarra A. 2011. Effects of tropical cyclones on ocean heat transport in a high-resolution coupled general circulation model. *J. Clim.* **24**: 4368–4384. <https://doi.org/10.1175/2011jcli4104.1>.
- Sun Q, Miao C, Duan Q, Wang Y. 2015. Temperature and precipitation changes over the Loess Plateau between 1961 and 2011, based on high-density gauge observations. *Global Planet. Change* **132**: 1–10. <https://doi.org/10.1016/j.gloplacha.2015.05.011>.
- Taylor KE, Stouffer RJ, Meehl GA. 2012. An overview of CMIP5 and the experiment design. *Bull. Am. Meteorol. Soc.* **93**: 485–498. <https://doi.org/10.1175/BAMS-D-11-00094.1>.
- Timm OE, Giambelluca TW, Diaz HF. 2015. Statistical downscaling of rainfall changes in Hawai'i based on the CMIP5 global model projections. *J. Geophys. Res.* **120**: 92–112. <https://doi.org/10.1002/2014JD022059>.
- Voldoire A, Sanchez-Gomez E, Salas y Mélia D, Decharme B, Casou C, Sénési S, Valcke S, Beau I, Alias A, Chevallier M, Déqué M, Deshayes J, Douville H, Fernandez E, Madec G, Maisonnave E, Moine MP, Planton S, Saint-Martin D, Szopa S, Tyteca S, Alkama R, Belamari S, Braun A, Coquart L, Chauvin F. 2013. The CNRM-CM5.1 global climate model: description and basic evaluation. *Clim. Dyn.* **40**: 2091–2121. <https://doi.org/10.1007/s00382-011-1259-y>.
- Volodin EM, Dianskii NA, Gusev AV. 2010. Simulating present-day climate with the INMCM4.0 coupled model of the atmospheric and oceanic general circulations. *Izv Atmos. Oceanic Phys.* **46**: 414–431. <https://doi.org/10.1134/S000143381004002X>.
- Wang L, Chen W. 2014. A CMIP5 multimodel projection of future temperature, precipitation, and climatological drought in China. *Int. J. Climatol.* **34**: 2059–2078. <https://doi.org/10.1002/joc.3822>.
- Wang Q, Fan X, Qin Z, Wang M. 2012. Change trends of temperature and precipitation in the Loess Plateau region of China, 1961–2010. *Global Planet. Change* **92**: 138–147. <https://doi.org/10.1016/j.gloplacha.2012.05.010>.
- Wang HJ, Chen HP, Liu JP. 2015. Arctic sea ice decline intensified haze pollution in eastern China. *Atmos. Oceanic Sci. Lett.* **8**: 1–9. <https://doi.org/10.3878/AOSL20140081>.
- Watanabe S, Hajima T, Sudo K, Nagashima T, Takemura T, Okajima H, Nozawa T, Kawase H, Abe M, Yokohata T, Ise T, Sato H, Kato E, Takata K, Emori S, Kawamiya M. 2011. MIROC-ESM 2010: model description and basic results of CMIP5-20c3m experiments. *Geosci. Model Dev.* **4**: 845–872. <https://doi.org/10.5194/gmd-4-845-2011>.
- Watanabe M, Suzuki T, Oishi R, Komuro Y, Watanabe S, Emori S, Takemura T, Chikira M, Ogura T, Sekiguchi M, Takata K, Yamazaki D, Yokohata T, Nozawa T, Hasumi H, Tatebe H, Kimoto M. 2010. Improved climate simulation by MIROC5: mean states, variability, and climate sensitivity. *J. Clim.* **23**: 6312–6335. <https://doi.org/10.1175/2010jcli3679.1>.

- Willmott CJ, Matsuura K. 2005. Advantages of the mean absolute error (MAE) over the root mean square error (RMSE) in assessing average model performance. *Clim. Res.* **30**: 79–82. <https://doi.org/10.3354/cr030079>.
- Xin XG, Wu TW, Li JL, Wang ZZ, Li WP, Wu FH. 2013. How well does BCC_CSM1.1 reproduce the 20th century climate change over China? *Atmos. Oceanic Sci. Lett.* **6**: 21–26. <https://doi.org/10.1080/16742834.2013.11447053>.
- Xu J, Gao Y, Chen D, Xiao L, Ou T. 2017. Evaluation of global climate models for downscaling applications centred over the Tibetan Plateau. *Int. J. Climatol.* **37**: 657–671. <https://doi.org/10.1002/joc.4731>.
- Yukimoto S, Adachi Y, Hosaka M, Sakami T, Yoshimura H, Hirabara M, Tanaka TY, Shindo E, Tsujino H, Deushi M, Mizuta R, Yabu S, Obata A, Nakano H, Koshiro T, Ose T, Kitoh A. 2012. A new global climate model of the Meteorological Research Institute: MRI-CGCM3 – model description and basic performance. *J. Meteorol. Soc. Jpn.* **90A**: 23–64. <https://doi.org/10.2151/jmsj.2012-A02>.
- Zhang X, Wang Q, Mu M. 2017. The impact of global warming on Kuroshio Extension and its southern recirculation using CMIP5 experiments with a high-resolution climate model MIROC4h. *Theor. Appl. Climatol.* **127**: 815–827. <https://doi.org/10.1007/s00704-015-1672-y>.
- Zhou T, Song F, Chen X. 2013. Historical evolution of global and regional surface air temperature simulated by FGOALS-s2 and FGOALS-g2: how reliable are the model results? *Adv. Atmos. Sci.* **30**: 638–657. <https://doi.org/10.1007/s00376-013-2205-1>.
- Zhou B, Wen QH, Xu Y, Song L, Zhang X. 2014. Projected changes in temperature and precipitation extremes in China by the CMIP5 multimodel ensembles. *J. Clim.* **27**: 6591–6611. <https://doi.org/10.1175/JCLI-D-13-00761.1>.